

Lawrence Berkeley National Laboratory

LBL Publications

Title

Dissociate lattice oxygen redox reactions from capacity and voltage drops of battery electrodes

Permalink

<https://escholarship.org/uc/item/10c63797>

Journal

Science Advances, 6(6)

ISSN

2375-2548

Authors

Wu, Jinpeng
Zhuo, Zengqing
Rong, Xiaohui
et al.

Publication Date

2020-02-07

DOI

10.1126/sciadv.aaw3871

Peer reviewed

1 Title

2 Dissociate Lattice Oxygen Redox Reactions from Capacity and 3 Voltage Drops of Battery Electrodes

5 Authors

6 Jinpeng Wu,^{1,2,3} Zengqing Zhuo,^{4,2} Xiaohui Rong,⁵ Kehua Dai,^{6,2} Zachary
7 Lebens-Higgins,^{7,2} Shawn Sallis,^{8,2} Feng Pan⁴, Louis F. J. Piper,⁷ Gao Liu,⁸ Yi-de
8 Chuang,² Zahid Hussain,² Qinghao Li,^{5*} Rong Zeng,^{9*} Zhi-xun Shen,^{1,3,10*} Wanli
9 Yang^{2*}

11 Affiliations

12 1. Geballe Laboratory for Advanced Materials, Stanford University,
13 Stanford, California 94305, USA

14 2. Advanced Light Source, Lawrence Berkeley National Laboratory,
15 Berkeley, California 94720, USA

16 3. Stanford Institute for Materials and Energy Sciences, SLAC National
17 Accelerator Laboratory, Menlo Park, CA 94025, USA

18 4. School of Advanced Materials, Peking University Shenzhen Graduate
19 School, Shenzhen 518055, China

20 5. Key Laboratory for New Energy Materials and Devices, Institute of
21 Physics, Chinese Academy of Sciences, School of Physical Sciences,
22 University of Chinese Academy of Sciences, Beijing 100190, China

23 6. School of Metallurgy, Northeastern University, Shenyang 110819,
24 China

25 7. Department of Physics, Applied Physics and Astronomy, Binghamton
26 University, Binghamton, New York 13902, USA

27 8. Environmental Energy Technologies Division, Lawrence Berkeley
28 National Laboratory, Berkeley, California 94720, USA

29 9. Department of Electrical Engineering, Tsinghua University, Beijing
30 100084, China

31 10. Department of Physics and Applied Physics, Stanford University,
32 Stanford, California 94305, USA

33 * Correspondence to (QL) lqh@iphy.ac.cn, (RZ)
34 zengrong@tsinghua.edu.cn, (ZS) zxshen@stanford.edu, (WY)
35 wlyang@lbl.gov

37 One-sentence Summary

38 Lattice oxygen redox is not responsible for the capacity and voltage
39 decay in battery electrodes.

41 Abstract

42 The oxygen redox (OR) reaction is a promising concept for improving
43 battery energy density, however, oxygen activities are generally

44 considered detrimental to the stability and kinetics of batteries. Studies
45 of OR activities often mix the lattice OR with other oxygen-involved
46 reactions, such as gas release, radical oxygen evolution and surface
47 reactions, further shadowing the true property of the practically
48 meaningful lattice OR activities. Here, based on high-efficiency mapping
49 of resonant inelastic X-ray scattering (mRIXS) of both the transition-
50 metals and oxygen, we distinguish and quantify the lattice OR activities
51 in $\text{Na}_{0.6}[\text{Li}_{0.2}\text{Mn}_{0.8}]\text{O}_2$. Through the comparison with $\text{Na}_{2/3}[\text{Mg}_{1/3}\text{Mn}_{2/3}]\text{O}_2$
52 that also displays very strong lattice OR but distinct electrochemical
53 stability, our results unambiguously show that the significant capacity
54 drop in $\text{Na}_{0.6}[\text{Li}_{0.2}\text{Mn}_{0.8}]\text{O}_2$ stems from non-lattice-OR activities while
55 lattice OR remains strong and stable. Furthermore, the quantified Mn
56 redox reaction shows opposite trends in the two systems and significant
57 increase upon cycling in $\text{Na}_{0.6}[\text{Li}_{0.2}\text{Mn}_{0.8}]\text{O}_2$, leading directly to a
58 dramatically lowered discharge voltage. Our comparative study of the
59 two strong lattice OR systems with distinct electrochemical stability
60 suggests that lattice OR itself is not the ringleader of the stability issue
61 as conventionally believed. Instead, other irreversible oxygen activities
62 and the likely associated growth of cationic reactions lead to the
63 capacity and voltage fade. Distinguishing lattice OR from other oxygen
64 activities is critical for revealing the true property of oxygen redox
65 reactions, something that has not been emphasized enough. Many
66 intriguing findings and thoughts are triggered by this critical
67 clarification. We argue that lattice OR and other oxygen activities
68 should/could be treated separately to achieve viable OR-based
69 electrodes for high-performance batteries.

70

71 **MAIN TEXT**

72 **Introduction**

73 The demand for high-performance energy storage in today's
74 sustainable energy applications, especially electric vehicles and power
75 grid, requires both conceptual breakthroughs and practical
76 developments of batteries (1). Conventionally, only transition-metal
77 (TM) redox in oxide cathodes are considered practical in positive
78 electrodes, because oxygen activities trigger various stability and
79 voltage limit issues in batteries (2, 3). Such a conceptual barrier has
80 been complimented by recent scrutinies of oxygen activities, which
81 suggest that it could be possible to utilize reversible lattice oxygen
82 redox (OR) reactions to achieve high energy-density Li-ion and Na-ion
83 batteries (4-6). However, technical challenges on practical
84 employments of OR reactions remain formidable. While the
85 employment of this concept relies on reversible OR reactions in the bulk
86 lattice, hereafter called "*lattice OR*", electrochemically active oxygen
87 often seems to display inherent irreversibility and sluggish kinetics,
88 which trigger performance decays in both capacity and discharge
89 voltages (5, 7, 8).

90 Although extensive studies and debates on OR activities in battery
91 electrodes have been reported and reviewed (5), few has tried to
92 distinguish the practically meaningful “lattice-OR” from other
93 irreversible oxygen activities such as oxygen gas release, radical
94 oxygen evolution, and associated surface reactions, which were
95 reported in many literature especially for Li-rich materials(9-17). As
96 illustrated in literatures for both Li- and Na- ion systems, these
97 irreversible oxygen activities take place mostly on the electrode surface
98 and are directly associated with the surface configuration through
99 unclear mechanism (10, 15, 16). For clarity of discussions, hereafter,
100 we call such irreversible oxygen-oxidation “*non-lattice OR*” in this work;
101 however, we note that this designation is just for being consistent with
102 previous literature. In reality, such oxygen activities involve only
103 irreversible oxygen oxidation, which are not “red-ox” activities and
104 should not be called oxygen “redox” at all.

105 So far, OR chemistry has been mostly studied and discussed without
106 clear differentiation between lattice and non-lattice OR activities
107 defined above. A common approach to access OR reactions is based on
108 transition-metal measurements, because OR could be naturally invoked
109 if the cationic redox reactions cannot compensate the electrochemical
110 capacity. Although this is valid for evaluating the total OR activities, the
111 results could only represent a mixed contribution from both (reversible)
112 lattice OR and (irreversible) non-lattice OR (oxidation), so the true
113 properties of the critical lattice OR reactions cannot be distinguished
114 and disclosed. Endeavors trying to probe OR reactions more directly
115 were mostly based on popular oxygen spectroscopy of O-K XPS and
116 absorption, which encounter technical limitations on probe depth and
117 entangled signals (18). Nonetheless, several works have attempted to
118 disentangle the different activities in OR systems (19-22). It is clear
119 through these efforts that the contributions from lattice and non-lattice
120 OR activities are highly material dependent. Some systems display
121 almost purely lattice OR, e.g., $\text{Na}_{2/3}\text{Mg}_{1/3}\text{Mn}_{2/3}\text{O}_2$ (NMMO) and
122 $\text{Na}_{2/3}\text{Mg}_{0.28}\text{Mn}_{0.72}\text{O}_2$ (22, 23), while most other electrodes show significant
123 amount of non-lattice oxygen involvements, e.g., Li-rich compounds (9-
124 14). Due to the irreversible nature of the non-lattice OR, without
125 differentiating the lattice OR from non-lattice OR activities, the critical
126 question on how lattice OR affects the electrochemical performance
127 remains elusive. However, the unique property of the NMMO material
128 with almost purely lattice OR provides an excellent opportunity for a
129 comparative study with another analog system with both lattice and
130 non-lattice OR reactions, which inspires the detailed investigation of
131 $\text{Na}_{0.6}[\text{Li}_{0.2}\text{Mn}_{0.8}]\text{O}_2$ (NLMO) in this work.

132 Technically, the lack of clarification of the lattice OR activities is largely
133 due to the technical challenge on directly detecting and distinguishing
134 lattice-OR contributions from the other non-lattice OR and cationic
135 activities. Additionally, a reliable probe of lattice OR reactions requires
136 direct and quantitative detections of both the cationic (TM *3d*) and

137 anionic (O 2p) redox states in the bulk lattice. Such a technical
138 challenge has been solved only recently through the developments of
139 ultra-high efficiency mapping of resonant X-ray inelastic scattering
140 (mRIXS) technique and data-analysis methodologies (18, 22, 24). For
141 cationic redox reactions, mRIXS solves the TM-L distortion issue in
142 conventional absorption spectroscopy through the inverse partial
143 fluorescence yield (iPFY) with high enough energy resolution (24).
144 Compared with hard X-ray TM-K absorption spectroscopy, mRIXS-iPFY is
145 a direct detection of the TM-3d valence states with about 200 nm probe
146 depth for most TM L-edges (25). The direct 3d detection is sensitive
147 enough for quantitative analysis of almost all the relevant TM oxidation
148 states (18, 26). For reactions involving oxygen, mRIXS successfully
149 fingerprints the lattice OR reactions through a specific feature at 523.7
150 eV emission energy(18, 22, 27, 28). The emission energy of this feature
151 matches the spectroscopic signature of oxidized oxygen, which was
152 found to be from excitations to unoccupied O 2p states, i.e., non-
153 divalent as O²⁻ has only fully occupied 2p states (29). The crucial
154 achievement through O-K mRIXS is that this lattice OR feature is
155 isolated from the broad TM-O hybridization features around 525 eV
156 emission energy that are long known to the physics community(30).
157 This difference in emission energy through mRIXS ultimately resolve the
158 entangled signals in conventional soft X-ray absorption spectroscopy
159 (sXAS) and distinguishes the lattice oxidized oxygen involved in lattice
160 OR reactions (18). Furthermore, because mRIXS reveals the full
161 spectroscopic profile of lattice OR reactions along both the excitation
162 and emission energies, an intensity integration of the critical mRIXS
163 feature through the super-partial fluorescence yield (sPFY) analysis
164 could quantify the variation of oxidized oxygen in electrodes (22).
165 Additionally, the irradiation effect has also been carefully checked and
166 the oxidized oxygen mRIXS feature in battery electrodes could only be
167 eliminated by high-flux radiation, which directly rules out the possibility
168 of photon-induced mRIXS feature of oxidized oxygen(31). The mRIXS
169 observation of the oxidized oxygen is thus intrinsic, and could at worst
170 be underestimated if the beam flux is not carefully controlled (see
171 “Materials and Methods”). Therefore, these recent technical and
172 methodological developments and demonstrations have established the
173 combined TM-L mRIXS-iPFY and O-K mRIXS-sPFY analysis as so far the
174 most direct and quantitative probes of both cationic and anionic redox
175 states in batteries(18, 22, 27, 28).

176 mRIXS-based quantifications of the lattice OR activities in NMMO and Li-
177 rich Li_{1.17}Ni_{0.21}Co_{0.08}Mn_{0.54}O₂ compounds have shown an intriguing
178 phenomenon: lattice OR could display high reversibility in electrode
179 systems with or without other non-lattice oxygen activities (22).
180 Because non-lattice OR reactions, e.g., gas release and surface
181 reactions of radical oxygen, are irreversible, such a finding questions
182 our common understanding of OR effects on electrochemistry, and it
183 becomes vital and practically meaningful to clarify whether lattice OR is
184 associated with the electrochemical decay. Such a clarification could be

185 achieved through detailed and quantitative comparison between NMMO
186 and another analog system, NLMO here, both with strong OR reactions,
187 but with distinct electrochemical decays in the capacity and discharge
188 voltage.

189 In this work, we quantitatively analyze both the lattice OR and Mn redox
190 in $\text{Na}_{0.6}[\text{Li}_{0.2}\text{Mn}_{0.8}]\text{O}_2$ (NLMO) with the focus on clarifying the effects of
191 oxygen activities on electrochemistry. NLMO involves only one cationic
192 (Mn) and one anionic (O) possible charge transfer site, therefore, could
193 be directly compared with NMMO. Contrasting the NMMO system that
194 displays a relatively stable electrochemical (22), NLMO system shows
195 dramatic capacity fade and a fast-growing discharge plateau at a low
196 voltage in only 12 cycles (Fig. 1). Because both NMMO and NLMO
197 display strong lattice OR reactions, such a clear electrochemical
198 contrast provides direct evidence to decouple the lattice OR from the
199 capacity and voltage decay. Through Mn-L mRIXS-iPFY and O-K mRIXS-
200 sPFY quantifications, both the lattice OR and bulk Mn redox
201 contributions to electrochemistry are quantified in NLMO. Our
202 experimental results reveal a surprisingly high reversibility (97%) of the
203 lattice OR during the initial cycle of NLMO, resembling that in NMMO.
204 However, a large amount (34%) of the oxygen oxidation during the
205 initial charge are found due to the irreversible non-lattice OR, which
206 contrasts NMMO and is responsible for the capacity loss in general.
207 Additionally, bulk Mn redox starts to emerge from the initial discharge
208 and grows significantly upon cycling, with Mn-capacity contribution
209 almost doubled within only 12 cycles, again contrasting the relatively
210 stable Mn redox contribution in NMMO after 100 cycles. The growing Mn
211 redox corresponds to the development of lower-voltage discharge
212 plateau in NLMO system. Our results unambiguously show that capacity
213 and voltage drops are not inherent problems of lattice OR activities.
214 Instead, the majority of the capacity decay in OR systems is due to non-
215 lattice OR reactions, while the growing cationic redox upon cycling is
216 responsible for the low-voltage plateau during discharge. This critical
217 clarification triggers many intriguing questions for future researches
218 and developments.

219 Results

220 **Materials and electrochemistry.** The P3-type $\text{Na}_{0.6}[\text{Li}_{0.2}\text{Mn}_{0.8}]\text{O}_2$ is
221 synthesized by a solid-state reaction as reported previously (32). The
222 electrochemical performance has been extensively studied as shown in
223 Fig. S1. The structure of the material was studied by XRD (Fig. S2). The
224 morphology of the particles studied by SEM (Fig. S3) shows that the
225 particles are of the size less than 7 μm (32). Compared with P2-type
226 NMMO, the NLMO studied here is of the different P3-type stacking
227 sequence (Fig. 1) (32-35). Otherwise, the major difference between the
228 two systems is only on the dopants in the TM-O layer, i.e., Li in NLMO
229 and Mg in NMMO. This work focuses on ten representative NLMO
230 samples with different states of charge (SOC) from 1, 2, and 12 cycles,
231 as marked in Fig. 1A. Samples are named as (cycle-number)C/D(voltage)

232 value), with “C” and “D” corresponding to charging and discharging
233 processes, respectively, e.g., 1C4.5 represents an electrode after the 1st
234 cycle (1) charging (“C”) to 4.5 V (4.5) voltage.

235 Previous studies have reached the agreement that significant amount
236 of OR activities are involved in the cycling of both NMMO and NLMO
237 systems due to the nominal high-valence Mn⁴⁺ in pristine materials due
238 to Li/Mg doping (33-36). However, as shown in Fig. 1, the NMMO and
239 NLMO display very different electrochemical profile. The NLMO
240 electrodes display a significant capacity drop and a growing low-voltage
241 discharge plateau within only tens of cycles, providing a unique system
242 to study these electrochemical performance decay in a OR dominating
243 system.

244 **Quantification of bulk Mn redox through mRIXS-iPFY.** As
245 reviewed before (25, 26), sXAS of TM-L edges provide the most direct
246 and quantitative detections of the TM-3d valence states. For Mn,
247 absolute values of valence distributions at different electrochemical
248 states can be directly quantified through a straightforward linear
249 combination fitting of the Mn^{2+/3+/4+} reference spectra (37).
250 Unfortunately, although sXAS could typically be collected in both total
251 electron yield (TEY) and total fluorescence yield (TFY) modes with probe
252 depth of 10 and 100 nm, respectively (38), Mn-L sXAS in the bulk-
253 sensitive TFY mode encounters serious lineshape distortions due to the
254 significant signal contributions from oxygen in the samples (24, 39),
255 hindering reliable quantifications. As shown in Fig. S4, Mn-L TFY spectra
256 are seriously distorted and cannot be used for quantifying the bulk Mn
257 redox reactions. Therefore, we employ Mn-L mRIXS-iPFY to probe the
258 bulk Mn valence states. The principle of iPFY through energy-resolved
259 fluorescence signals has been explained by Achkar *et al.* through Silicon
260 drift detectors, and has been demonstrated to be a non-distorted bulk-
261 sensitive probe of TM-L edges (39). Here, we extract Mn-L iPFY signals
262 from mRIXS (Fig. 2) by integrating the fluorescence signals from oxygen
263 with emission energy range of 475-525 eV (Fig. 2B). We note that the
264 energy resolution of our mRIXS results are several hundred times
265 higher than silicon drift detectors in previous iPFY studies, leading to a
266 clear separation between the emission signals from O (around 520 eV
267 emission energy) and Mn (around 640 eV emission energy) for
268 extracting clean iPFY spectra (18, 24).

269 Fig. 2A shows the iPFY Mn-L spectra (solid lines) of the representative
270 NLMO electrodes at different electrochemical states at each cycle.
271 mRIXS images and mRIXS-iPFY spectra of all the electrodes are
272 presented in Fig. S5 and Fig. S6, respectively. The non-distorted Mn-L
273 iPFY enables quantitative analysis of the Mn valence states in the bulk
274 at different electrochemical states through the established linear
275 combination fitting based on the Mn reference spectra (40). The fitting
276 ones (dotted lines in Fig. 2A) completely overlap with our experimental

277 iPFY data (solid lines in Fig. 2A), indicating a precise quantification of
278 the Mn oxidation states with the values summarized in Table 1.

279 In general, Mn⁴⁺ dominates the bulk signal of most electrodes studied
280 here, which is expected by considering the NLMO stoichiometry with
281 only nominal Mn⁴⁺ in pristine materials. However, a weak but clear
282 variation around 641.5 eV at different electrochemical states, with the
283 intensity growing upon cycling, indicates a finite amount of Mn³⁺
284 developed in the system. Such an evolution of Mn states is clearly
285 revealed through the quantification analysis (Table 1) that is visualized
286 in Fig. 2C.

287 The tiny capacity before the initial charge plateau corresponds to a
288 small drop (increase) of Mn³⁺ (Mn⁴⁺) contents (Table 1), indicating a
289 trace amount of Mn³⁺ exists in the pristine material from sample
290 preparation and is oxidized to Mn⁴⁺ at the beginning of the 1st charge.
291 Throughout the long charge (4.25 V) and discharge (4.0 V) plateau, the
292 Mn remains Mn⁴⁺. However, Mn³⁺ starts to emerge below 3.95 V during
293 discharge with a decreasing amount of Mn⁴⁺, revealing that Mn^{3+/4+}
294 redox reactions contribute to the short low-voltage discharge plateau
295 around 3.8 V. More importantly, upon electrochemical cycling, the
296 quantified contributions from Mn^{3+/4+} redox reactions continuously
297 increase upon cycling and the average Mn valence state drops
298 significantly with 15% Mn³⁺ in discharged electrode after only 12 cycles
299 (Table 1, Fig. 2C).

300 Therefore, our quantitative analysis based on Mn-L mRIXS-iPFY clearly
301 reveals the evolving Mn^{3+/4+} redox in the bulk upon electrochemical
302 operations: i) Mn^{3+/4+} redox emerges from the first discharge cycle. ii)
303 Contributions from Mn redox grow upon cycle numbers. iii) The overall
304 Mn valence states drop significantly in NLMO after only 12 cycles. The
305 quantified oxidation states of Mn directly correspond with the electron
306 charge numbers, and the electrochemical capacity associated with Mn
307 redox can be calculated based on Nernst Equation, as provided in Table
308 1. It is clear that the quantified Mn redox contribution matches the
309 electrochemical capacity during the discharge 3.8 V plateau, leading to
310 a continuous voltage drop upon cycling.

311 More importantly, such a dramatic development of Mn redox with only
312 12 cycles is in sharp contrast with the NMMO system, where Mn redox
313 contributions to electrochemistry remain the same level after a hundred
314 cycles (22).

315 **Surface and Irreversible Reactions in NLMO.** Another critical
316 finding, based on Mn-L quantifications, is from the surface-sensitive
317 sXAS-TEY signal. As shown in Fig. 2A and Fig. S4, surface TEY contrasts
318 bulk mRIXS-iPFY spectra with a clear signature of Mn²⁺, which could be
319 directly seen in the raw data of Mn-L sXAS plots through the low-energy
320 peak at about 640 eV. On the one hand, the sharp contrast between the

321 surface-sensitive TEY and mRIXS-iPFY indicates that the signals of
322 mRIXS-iPFY are indeed dominated by the bulk information. On the other
323 hand, these surface-sensitive TEY spectra could also be precisely fitted
324 through linear combinations of the references (26, 37, 40), with the
325 values given in Table 1 and visualized in Fig. 2C.

326 Strikingly, during the charge (oxidation) process, the low-valence Mn^{2+}
327 content increases significantly on surface and reaches the maximum
328 value at the fully charged state (Table 1 and Fig. 2C). Such a
329 counterintuitive behavior of the enhancing surface Mn^{2+} during charge
330 has been found in high-voltage Li-ion battery electrodes, suggesting
331 significant surface reactions taking place during the high-potential
332 charge involving electrolyte degradation (41). It is important to note
333 that, although surface Mn^{2+} development could be seen in Na-ion
334 battery electrodes (22, 37), the activity typically follows the expected
335 reduction process during discharge. In direct contrast, NMMO displays
336 an enhanced Mn^{2+} concentration during discharge as expected (22).
337 Therefore, the reversed behavior of surface Mn^{2+} upon SOCs in NLMO is
338 a clear signature of strong surface reactions. For systems involving
339 electrochemically activated oxygen, such a surface behavior resembles
340 the typical Li-rich compounds that often displays surface condensation
341 and TM reduction after high-voltage charging because of both the
342 oxygen release and surface reactions involving electrolyte(10-14, 17).

343 The oxygen release and surface reactions have been extensively
344 studied in Li-rich layered compounds, although many questions remain
345 open (10-14). In general, it is believed that, during the high voltage
346 charging, many different types of side reactions could take place on the
347 electrode surface, including the decomposition of the electrolyte itself
348 and the surface carbonates. Additionally, oxygen could be released
349 from the electrode materials, in the form of either O_2 gas or radical
350 oxygen, $\cdot O_2$, which is highly reactive with the electrolyte on the
351 electrode surface (11, 17). These studies have also shown that TM
352 reduction is directly associated with these side reactions (11).

353 Indeed, a very recent work by Bruce *et al.* on gas release studies shows
354 that the NLMO system shows O_2 gas release and radical O evolution at
355 very high voltage, contrasting the relatively stable NMMO system (15).
356 Their work also suggests that both of the oxygen release and radical
357 oxygen evolution take place on the surface within about 10 nm of
358 depth. The contrasting surface Mn^{2+} behaviors in NLMO and NMMO
359 systems described in this work are generally consistent with the gas
360 release findings, because oxygen release will lead to the reduction of
361 TMs especially in the surface regime (11). Therefore, the
362 counterintuitively enhanced surface Mn^{2+} signals in the charged state of
363 NLMO indicates that the irreversible non-lattice oxygen redox, which
364 takes place mostly in the surface regime in the forms of oxygen release
365 and surface reactions, is much stronger compared with NMMO. We note

366 that such a conclusion is directly supported by our lattice O redox
367 quantification results below.

368 **Quantification of Lattice O redox through mRIXS-sPFY.** The
369 quantifications of Mn redox reactions suggest that Mn redox contributes
370 to only a very limited amount of electrochemical capacity. This is
371 expected as NLMO should be a strong OR system due to the high-
372 valence Mn in its pristine state. However, although the OR reactions are
373 supposed to dominate the electrochemical cycling, pre-edge features of
374 O-K sXAS display only a small change at different electrochemical
375 states in both TEY and TFY modes (Fig. S7). As a matter of fact, we
376 have recently clarified that the variation of the O-K sXAS pre-edges is
377 dominated by the changes of TM-O hybridization, not OR reactions (18).
378 Therefore, as introduced earlier, O-K mRIXS is capable of isolating the
379 lattice OR signature from the strong hybridization features and is thus
380 employed here to detect and quantify the lattice OR reactions through
381 previously demonstrated methodologies (18, 22, 27, 42).

382 Fig. 3 displays the mRIXS and sPFY results of all the representative
383 NLMO electrodes at different cycling states, with samples indicated in
384 Fig. 1. It is clear that the signature of the oxidized oxygen at 523.7 eV
385 emission and 531 eV excitation energies emerges with the 4.25 V
386 charge plateau, and disappears after the 4 V discharge plateau (red
387 arrows in Fig. 3A). This defines a voltage boundary of lattice OR
388 reactions, and is consistent with the aforementioned analysis on Mn
389 redox reactions, which display Mn-L spectroscopic variations only
390 outside the OR voltage range (Table 1, Fig. 2C). Therefore, unlike most
391 Li-ion compounds, e.g., Li-rich electrodes, where TM and O redox are
392 often mixed together during discharge (19, 27), the cationic and anionic
393 redox reactions in NLMO takes place at different potential ranges, the
394 same as NMMO system (22). An interesting question is whether the
395 separated (mixed) redox reactions are somehow more inherent to Na-
396 ion (Li-ion) electrodes, which deserves further studies of other electrode
397 materials. Nonetheless, the mRIXS results of O-K and Mn-L set an
398 electrochemical boundary of the two redox reactions, which will be
399 used later as one of the ways for quantifying the lattice OR
400 contributions to the electrochemical capacity.

401 Compared with O-K sXAS and/or individual RIXS cuts, an mRIXS image
402 is able to detect the full profile of the oxidized oxygen along both the
403 excitation and emission energy energies (29), providing a unique
404 opportunity to quantify the complete spectroscopic intensity of the
405 oxidized oxygen states. Fig. 3B and 3C display the sPFY extracted by
406 integrating the intensity within the characteristic emission-energy
407 window around 523.7 eV (signals between the two dotted lines marked
408 on Fig. 3A). In this way, the specific oxygen redox mRIXS feature is
409 reduced to a 1D sPFY spectrum. The corresponding intensity around
410 531 eV excitation energy varies with electrochemical states (Fig. 3B),
411 with a peak and dip clearly shown in charged and discharged states

412 (Fig. 3C). The full intensity of oxidized oxygen feature could then be
413 quantified by a simple area integration of the mRIXS-sPFY within 530-
414 532 eV energy (see “Materials and Methods”).

415 The quantified mRIXS-sPFY intensities at different SOCs are presented
416 in Table 2 and plotted in Fig. 4A on top of the electrochemical profile.
417 First, it is clear that strong lattice OR reactions take place during the
418 long charge and discharge plateaus. Mn redox, colored as blue, was
419 quantified independently above (Table 1, Fig. 2C) and dominates the
420 capacity outside these two high-voltage plateaus. Second, the mRIXS-
421 sPFY peak area changes during initial charge (0.232) and discharge
422 (0.224) suggests a highly (97%) reversible lattice OR reactions during
423 the initial cycle, even higher than that in NMMO (79%) (22). Third,
424 contrasting the highly reversible lattice OR reaction during the initial
425 cycle, the electrochemical profile shows a significant capacity drop of
426 the overall OR plateaus from charging (105.1 mAh/g) to discharging
427 (66.6 mAh/g). This sharp contrast indicates that the strong lattice OR
428 reactions and the loss of capacity are not strongly associated.
429 Additionally, this also implies that a large portion of the overall OR
430 contributions is not from lattice OR, which is consistent with the strong
431 surface activities during charging. We therefore pursue a more detailed
432 analysis to differentiate the lattice OR from other non-lattice OR
433 contributions.

434 A relationship between the electrochemical capacity and the mRIXS-
435 sPFY peak area change is needed to quantify the lattice OR capacity.
436 Because studies show that the majority of non-lattice OR reactions take
437 place during the charging process (10-14), the O-K sPFY peak-area
438 change during discharge is therefore a more reliable probe of lattice
439 OR. We first assume and test a proportional relationship between the
440 sPFY peak-area change during discharge to the amount of lattice OR
441 reactions. Such a simple dependence has been verified by the perfect
442 match between electrochemical profile and sPFY peak area change in
443 NMMO with pure lattice OR reactions (22). For NLMO, we test the
444 validity of this linear dependence with the 1st, 2nd, and 12th discharging
445 processes, which display discharge capacities of 66.6, 59.5, and 39.7
446 mAh/g with the sPFY peak area changes of 0.224, 0.195, and 0.130,
447 respectively. Therefore, the three tested discharge cycles consistently
448 show a ratio between lattice OR capacity and sPFY peak area change,
449 i.e., 303, 305, and 305 mAh/g per peak-area change during the 1st, 2nd,
450 and 12th discharge. Considering the slight broadening of spectroscopic
451 features upon cycling from structural amorphization, these values are
452 highly consistent, confirming that discharge capacity is indeed
453 dominated by lattice OR with a quantification ratio of about 303 mAh/g
454 per peak area change. Based on this self-consistent analysis and the
455 conversion ratio, the quantified capacity from the lattice OR
456 contribution at each discharge cycle is provided in Table 2, and
457 visualized in Fig. 4B as the “mRIXS” results (narrow bars).

458 Discussions

459 **Joint quantification results of Mn and O redox reactions.** Based
460 on the Mn-L mRIXS-iPFY and O-K mRIXS-sPFY results, we have now
461 achieved two sets of quantified capacity from the Mn and O redox in
462 NLMO. i) The Mn (Fig. 2C) and O (Fig. 4A) spectroscopic changes set the
463 boundary between the cationic and anionic redox reactions, so
464 electrochemical capacities can now be defined to specific redox
465 reactions (Method-I). The values are plotted in Fig. 4B as framed wide
466 columns from “electrochemistry”. ii) The absolute values of electron
467 charge transfer, as well as the capacity, from Mn redox can be
468 calculated purely based on the Mn oxidation states quantified through
469 Mn-L mRIXS-iPFY (Table 1). For OR contributions, the capacity could
470 also be calculated based on the O-K sPFY peak area changes and the
471 conversion ratio of 303 mAh/g per peak-area change, as detailed above
472 (Method-II). The independently quantified Mn and lattice OR capacities
473 from spectroscopy are also plotted in Fig. 4B as “mRIXS” results beside
474 the electrochemistry results.

475 **Low-voltage plateau with growing Mn redox.** Fig. 4B visualizes the
476 quantification results of Mn and lattice-O redox during the discharging
477 process based on the two different methods. It is obvious that the
478 quantifications from electrochemistry (Method-I) are in great agreement
479 with the values from mRIXS-iPFY (for Mn redox) and mRIXS-sPFY (for
480 lattice OR) results (Method-II). Additionally, Fig. 4B shows that, after
481 only 12 cycles, the lattice OR capacity drops; however, the Mn redox
482 contribution almost doubles. Note the $\text{Mn}^{3+/4+}$ redox contributions from
483 Method-II are absolute values of electron charge transfer numbers
484 purely based on spectroscopic results (Table 1). Therefore, the match
485 between the Mn redox contributions from Method-II (purely
486 spectroscopy) and the capacities of the low-voltage discharge plateau
487 concludes that the growing low-voltage plateau during discharge is due
488 to the continuously increasing $\text{Mn}^{3+/4+}$ redox upon cycling.

489 Very recently, the increasing cationic redox in Li-rich compounds was
490 proposed as the central mechanism of voltage fade of Li-rich electrodes
491 (7). Here, the NLMO shows a much clearer low-voltage reaction that
492 grows upon cycling, and our quantification results experimentally
493 conclude that this growing low-voltage reaction is due to $\text{Mn}^{3+/4+}$ redox
494 reactions developed upon cycling of this Na-ion system. More
495 importantly, contrasting these NLMO findings, the Mn redox capacities
496 remain stable even after 100 cycles in NMMO, which also displays
497 strong lattice OR reactions (22). Therefore, the contrast on the stability
498 of Mn redox and the discharge voltage are not due to the strong lattice
499 OR activities that exist in both NLMO and NMMO systems.

500 **Capacity loss with non-lattice OR.** While the discharge capacity
501 could be well understood through the mRIXS quantifications of Mn and
502 lattice OR reactions (Fig. 4B), the charging capacity significantly
503 deviates from the mRIXS quantifications (Fig. 4C). This is consistent

504 with the strong surface reactions on NLMO as discussed above. In
505 general, oxygen evolves from the NLMO during high-voltage charging in
506 the form of gas release and/or radical oxygen, leading to irreversible
507 surface reactions with CO₂ gas release (15). Such non-lattice OR
508 activities are highly irreversible, i.e., they behave very differently from
509 the reversible lattice OR detected in our mRIXS experiments. The
510 quantitative comparison between the electrochemical capacity defined
511 by method-I and the mRIXS quantifications through method-II shows
512 that about 36.1 mAh/g capacity is from irreversible non-lattice OR
513 contributions during initial charge (Fig. 4C). In addition to the capacity
514 plots here, the quantification results in electron charge transfer
515 numbers is provided in Fig. S8.

516 A striking finding emerges from the quantitative analysis of the
517 charging process (Fig. 4C). With the lattice OR reactions being highly
518 reversible (69 and 66.6 mAh/g during initial charge and discharge), the
519 irreversible non-lattice OR activities almost fully cover the capacity loss.
520 For example, the initial-cycle OR capacity loss is 105.1 (charge) - 66.6
521 (discharge) = 38.5 mAh/g (Fig. 4 B & C), or 0.131 (0.358 - 0.227)
522 electron charge transfer (Fig. S8). This loss of capacity is dominated by
523 the non-lattice OR contribution (36.1 mAh/g), plus only a very small (2.4
524 mAh/g) decay of lattice-OR contribution. The loss of OR capacity is
525 compensated by the emerging Mn redox (8.9 mAh/g) during discharge,
526 leading to the eventual value of 75.5 mAh/g discharge capacity. Such a
527 capacity loss from non-lattice OR continues in the following cycles, i.e.,
528 non-Lattice OR capacity (12.6 mAh/g) gets totally lost while lattice OR
529 maintain a decent reversibility during the 2nd cycle (60.4 mAh/g
530 charged, 58.0 mAh/g discharged, Fig. 4B, C). Therefore, the capacity
531 loss of NLMO are from three contributions: i) the irreversible non-lattice
532 OR dominates the loss of capacity; ii) lattice OR capacity drops only
533 slightly, less than 5%; iii) the loss from OR is compensated by the
534 emerging Mn redox, however, the Mn redox contribution remains much
535 lower than the lost non-lattice OR capacity, leading to the drop of the
536 total capacity.

537 The conclusion that capacity loss in NLMO is mainly from non-lattice OR
538 reactions is again consistent with the contrast between NLMO and
539 NMMO (Fig. 1). While both systems display strong lattice OR reactions,
540 the significant capacity loss takes place only in NLMO with significant
541 amount of non-lattice OR activities. Because only the reversible lattice
542 OR reaction dominates the cycling in NMMO (15, 22, 23), no significant
543 capacity drop is observed within 12 cycles.

544 **Intriguing relationships and perspectives.** This comparative study
545 concludes that the significant capacity loss of NLMO is not from lattice
546 OR reactions, and the low-voltage discharge plateau is from the
547 growing cationic (Mn) redox upon cycling, several complex and
548 intriguing relationships emerge from the observations here, which are
549 critical for future studies and material optimizations.

550 Firstly, on the voltage fade, compared with NMMO system with strong
551 lattice OR but stable Mn redox capacity for a hundred cycles (22), the
552 NLMO here shows significant increase of Mn redox contributions for only
553 12 cycles. Although both systems display strong lattice OR reactions,
554 NMMO shows almost purely lattice OR while NLMO features a large
555 amount of non-lattice OR reactions during charging (15, 23). This
556 indicates that the increasing Mn redox upon cycling is associated with
557 non-lattice OR reactions, as also suggested for Li-rich compounds very
558 recently (7). Secondly, even for NMMO system, voltage fade is
559 observed, most clearly after 50 cycles and was attributed to the
560 decrease of averaged Mn oxidation states (22). However, an interesting
561 coincident is that the most significant decrease of lattice OR also takes
562 place after 50 cycles there. This not only confirms that lattice OR itself
563 is not responsible for the dropping discharge voltage; on the contrary,
564 decreasing lattice OR reactions may be associated with part of the
565 voltage drop, i.e., lattice OR should be stabilized, not suppressed, to
566 maintain discharge voltage.

567 Thirdly, the practicability of the concept of lattice OR depends on how
568 reversible and stable the reaction could be. Aside from the high
569 reversibility of lattice OR during the initial cycle, the reaction displays a
570 poor cyclability in only 12 cycles with capacity dropping from 66.6 to
571 38.7 mAh/g based on mRIXS quantifications (Fig. 4B). A close inspection
572 shows that the loss of lattice OR capacity, corresponding to the
573 decreasing difference of the mRIXS-sPFY peak-area between the
574 charged and discharged states (Double arrows in Fig. 3C), is mostly
575 from the discharged states. The sPFY remains roughly stable in the
576 charged states (Table 2, Fig. 3C); however, the sPFY of discharged states
577 is obviously enhanced around 531 eV after only 12 cycles. This could be
578 seen directly through the sPFY spectra in Fig. 3C, which shows that the
579 intensity between 530-532 eV is clearly enhanced in the 12th discharged
580 state (green arrow in Fig. 3C), leading to the decrease of sPFY contrast
581 between the charged and discharged states. Such a change of
582 discharged states on lattice OR has also been seen in NMMO, however,
583 the effect there is weak and spectroscopic lineshape broadening upon
584 cycling cannot be ruled out (22). In NLMO, the change of sPFY intensity
585 in discharged states is strong and cannot be simply interpreted by
586 spectroscopic broadening upon cycling, i.e., discharged 12D3.5 displays
587 dedicated signals around 531 eV (green arrow) that cannot be from
588 peak broadening (Fig. 3C). Therefore, the sPFY here implies that the
589 poor cyclability of lattice OR in NLMO is likely because the oxidized
590 oxygen is not completely reduced back to O²⁻ in discharged states after
591 extended cycles. This finding is in sharp contrast to our common belief
592 that most reversibility and cyclability issues are associated with high-
593 voltage charging. In the meantime, such irreversibility at discharged
594 states could be associated with the increasing Mn redox activities upon
595 cycling in NLMO (Fig. 2 & 4). Fundamentally, a reshuffling of the Mn and
596 O electronic states is necessary to allow Mn redox to take place with
597 the continued existence of non-divalent oxygen, which interestingly

598 assembles the situation in Li-rich materials, where cationic redox
599 overlaps with OR reactions in a wide potential range during discharge
600 (27).

601 Fourthly, the initial-cycle reversibility of lattice OR is much higher in
602 NLMO (97%) than that in NMMO (79%) (22). Two differences between
603 the systems may be associated with this initial reversibility. One
604 unlikely scenario is that the significant amount of non-lattice oxygen
605 activities in NLMO may have changed the redox-active oxygen
606 configurations, as speculated above, and counterintuitively optimized
607 the stability of lattice OR. The other likely effect is the Li dopants in
608 NLMO, instead of the Mg in NMMO. Although both Li and Mg are
609 electrochemically inactive, the comparisons with NMMO in this work
610 have revealed that replacing Mg with Li changes all the three types of
611 redox activities in NLMO: the non-lattice OR (significant in NLMO),
612 lattice OR (better reversibility in NLMO), and Mn redox (growing upon
613 cycling in NLMO) reactions. The quantifications of the redox processes
614 here, not only contribute to further understandings the effect of Li and
615 Mn dopants; but also, the results show directly that dopants of
616 electrochemically inactive elements could change strongly the redox
617 related activities in batteries.

618 To fully understand the many intriguing findings here is in dire need of
619 the fundamental clarifications of the true driving force for activating
620 oxygen in TM oxide electrodes towards different redox activities, which
621 remains a grand challenge for future experimental and theoretical
622 studies. We also note that other important questions remain
623 unanswered, such as the relationship between lattice OR and surface
624 properties (9) and the kinetics that leads to the strong hysteresis in
625 NMMO (5, 43). Nonetheless, the key experimental conclusions of this
626 work on the capacity and voltage drop make important corrections to
627 our conventional wisdom. Our central results show that lattice OR itself
628 is not responsible for the performance decay, and the real ringleaders
629 are other irreversible oxygen activities. This means that it is critical to
630 distinguish lattice OR from other oxygen activities for clarifying the
631 concept of OR-based electrodes. The comparison between the two
632 materials, NLMO and NMMO, implies that different types of OR reactions
633 are intrinsic material properties, not simply the voltage range. This is
634 another critical information that deserves future works on more
635 systems to confirm and to clarify. Practically, the conclusions of this
636 work lead to different aspects on material optimizations: lattice OR
637 should/could be enhanced and maintained to be stable, e.g., through
638 lattice doping, but other oxygen activities should/could be suppressed,
639 e.g., through surface treatments. The combination of the two
640 approaches holds the promise towards viable OR-based high-
641 performance electrodes.

642

643 **Materials and Methods**

644 **Material synthesis and electrochemical test.** The P3-type
645 $\text{Na}_{0.6}[\text{Li}_{0.2}\text{Mn}_{0.8}]\text{O}_2$ electrode material was synthesized by a solid-state
646 reaction using precursor of Na_2CO_3 (99.9%, Alfa), LiOH (98%, Alfa), and
647 MnO_2 (99.9%, Alfa). The prepared electrode material was assembled
648 into CR2032 coin cells containing a metallic-Na anode, a glass-fiber
649 separator, a liquid electrolyte of 1M NaClO_4 in ethylene, dimethyl
650 carbonate (DMC), propylene carbonate (1:1:1 in volume), and
651 fluoroethylene carbonate (2% in volume, for improving the high voltage
652 cycle performance due to the higher redox potential than PC). The
653 electrochemical test was carried out using Land CT2001A battery test
654 system, in a voltage range of 3.5 - 4.5V at the rate of 0.1C (10 mAh g^{-1})
655 under room temperature. More details on materials and structural
656 characterizations were reported previously (32).

657 **Soft X-ray absorption spectroscopy (sXAS) and sample**
658 **handling:** sXAS measurement was performed in the iRIXS endstation
659 at Beamline 8.0.1 of the Advanced Light Source (ALS) at Lawrence
660 Berkeley National Laboratory (LBNL) (24). The electrode samples were
661 cut into small pieces (about 3mm×3mm) in the Ar glove box, and
662 pasted onto a sample holder. The sample holder was then loaded into a
663 specially-designed sample transfer mini-chamber. The mini-chamber
664 was then sealed, and mounted onto the iRIXS endstation under vacuum
665 for direct pump-down to avoid any air exposure. All the TEY and TFY
666 spectra were normalized to the beam flux measured by the upstream
667 gold mesh. The resolution of the excitation energy is 0.15 eV without
668 considering core-hole lifetime broadening. Refer to the previously
669 published work with detailed procedures (44).

670 **Mapping of resonant inelastic X-ray scattering (mRIXS).** mRIXS
671 was measured in the iRIXS endstation at Beamline 8.0.1 of ALS (24).
672 The beam spot size is about 25*100 μm (32). Additionally, in order to
673 increase the sampling across a large area of the electrode and to
674 reduce the radiation damage effect, data were collected with controlled
675 flux and itinerary samples throughout the measurements. Therefore,
676 the mRIXS signals represent the overall information of a large amount
677 of electrode materials. Considering the particle size of less than 7 μm ,
678 the area of mRIXS data collection covers thousands of particles.
679 Mapping data were collected by the ultra-high efficiency modular
680 spectrometer (45), with an excitation energy step of 0.2eV. The
681 resolution of the excitation energy is 0.35eV, and that of the emission
682 energy is 0.25eV. Final 2D maps were achieved via a multi-step data
683 processing including normalization to beam flux and collecting time,
684 integration and combination, etc., which has been elaborated in the
685 previous work (44).

686 **Mn-L inverse partial fluorescence yield (iPFY).** Mn-L iPFY was
687 achieved through the formula $\text{iPFY} = a/\text{PFY}_O$, where a is a
688 normalization coefficient, PFY_O is extracted by integrating the

689 fluorescence intensity within the O-K emission energy range (495 to
690 510 eV) on the Mn-L mRIXS (white square in Fig. 2B). Quantitative
691 fitting of Mn-L iPFY was performed via linear combination with the
692 standard experimental spectra of Mn^{2+/3+/4+}, as demonstrated and
693 detailed before (26).

694 **O-K super partial fluorescence yield (sPFY).** O-K sPFY was
695 achieved by integrating the mRIXS intensity within the emission energy
696 range of 523 to 524.5 eV (between dotted lines in Fig. 3A), where the
697 oxidized oxygen feature emerges. For quantification of the oxidized
698 oxygen feature, the area of the relevant sPFY feature was calculated by
699 integrating the intensity from 530 to 532 eV (shaded area in Fig. 3B,
700 3C), with a unitized 529.6 eV peak. The “Area Change” in Table 2 is the
701 difference on the integrated sPFY values between the charged and
702 discharged states at a particular cycle.

703 H2: Supplementary Materials

704

705 Fig. S1. Electrochemical performance of P3-type $\text{Na}_{0.6}[\text{Li}_{0.2}\text{Mn}_{0.8}]\text{O}_2$.

706 Fig. S2. Crystal Structural Evolution of $\text{Na}_{0.6}[\text{Li}_{0.2}\text{Mn}_{0.8}]\text{O}_2$.

707 Fig. S3. SEM images of the electrodes.

708 Fig. S4. Mn- L_3 sXAS (A) TEY and (B) TFY spectra.

709 Fig. S5. Mn- L_3 RIXS maps.

710 Fig. S6. Mn- L_3 mRIXS-iPFY spectra.

711 Fig. S7. O-K sXAS (A) TEY and (B) TFY spectra.

712 Fig. S8. Quantification of three different redox reactions in electron
713 charge transfer numbers.

714 Table S1. Linear fitting results of bulk Mn ions based on Mn- L_3 mRIXS-
715 iPFY.

716 Table S2. Linear fitting results of surface Mn ions based on Mn- L_3 TEY.

717References and Notes

718

7191. M. Armand, J. M. Tarascon, Building better batteries. *Nature* **451**, 652-720 (2008).
7212. J. B. Goodenough, Y. Kim, Challenges for Rechargeable Li Batteries. *Chemistry of Materials* **22**, 587-603 (2010).
7233. J. B. Goodenough, K.-S. Park, The Li-ion rechargeable battery: a perspective. *Journal of the American Chemical Society* **135**, 1167-1176 (2013).
7264. A. Grimaud, W. T. Hong, Y. Shao-Horn, J. M. Tarascon, Anionic redox processes for electrochemical devices. *Nat Mater* **15**, 121-126 (2016).
7285. G. Assat, J.-M. Tarascon, Fundamental understanding and practical challenges of anionic redox activity in Li-ion batteries. *Nature Energy* **3**, 373-386 (2018).
7316. X. Rong *et al.*, Anionic Redox Reaction-Induced High-Capacity and Low-Strain Cathode with Suppressed Phase Transition. *Joule* **3**, 1-15 (2018).
7337. E. Hu *et al.*, Evolution of redox couples in Li- and Mn-rich cathode materials and mitigation of voltage fade by reducing oxygen release. *Nature Energy* **3**, 690-698 (2018).
7368. A. Singer *et al.*, Nucleation of dislocations and their dynamics in layered oxide cathode materials during battery charging. *Nature Energy* **3**, 641-647 (2018).
7399. W. Yang, Oxygen release and oxygen redox. *Nature Energy* **3**, 619-620 (2018).
74110. S. E. Renfrew, B. D. McCloskey, Residual Lithium Carbonate Predominantly Accounts for First Cycle CO₂ and CO Outgassing of Li-Stoichiometric and Li-Rich Layered Transition-Metal Oxides. *J Am Chem Soc* **139**, 17853-17860 (2017).
74511. T. Hatsukade, A. Schiele, P. Hartmann, T. Brezesinski, J. Janek, Origin of Carbon Dioxide Evolved during Cycling of Nickel-Rich Layered NCM Cathodes. *ACS Appl Mater Interfaces* **10**, 38892-38899 (2018).
74812. T. Teufl, B. Strehle, P. Müller, H. A. Gasteiger, M. A. Mendez, Oxygen Release and Surface Degradation of Li- and Mn-Rich Layered Oxides in Variation of the Li₂MnO₃ Content. *Journal of The Electrochemical Society* **165**, A2718-A2731 (2018).
75213. A. R. Armstrong *et al.*, Demonstrating Oxygen Loss and Associated Structural Reorganization in the Lithium Battery Cathode Li[Ni_{0.2}Li_{0.2}Mn_{0.6}]O₂. *Journal of the American Chemical Society* **128**, 8694-8698 (2006).
75614. J. Hong *et al.*, Critical Role of Oxygen Evolved from Layered Li-Excess Metal Oxides in Lithium Rechargeable Batteries. *Chemistry of Materials* **24**, 2692-2697 (2012).
75915. R. A. House *et al.*, What Triggers Oxygen Loss in Oxygen Redox Cathode Materials? *Chemistry of Materials* **31**, 3293-3300 (2019).
76116. R. Jung, M. Metzger, F. Maglia, C. Stinner, H. A. Gasteiger, Oxygen Release and Its Effect on the Cycling Stability of LiNixMnyCozO₂ (NMC) Cathode Materials for Li-Ion Batteries. *Journal of The Electrochemical Society* **164**, A1361-A1377 (2017).

76517. J. Wandt, A. T. S. Freiberg, A. Ogorodnik, H. A. Gasteiger, Singlet oxygen evolution from layered transition metal oxide cathode materials and its implications for lithium-ion batteries. *Materials Today* **21**, 825-833 (2018).
- 766
- 767
- 768
76918. W. Yang, T. P. Devereaux, Anionic and cationic redox and interfaces in batteries: Advances from soft X-ray absorption spectroscopy to resonant inelastic scattering. *Journal of Power Sources* **389**, 188-197 (2018).
- 770
- 771
- 772
77319. G. Assat *et al.*, Fundamental interplay between anionic/cationic redox governing the kinetics and thermodynamics of lithium-rich cathodes. *Nat Commun* **8**, 2219 (2017).
- 774
- 775
77620. G. Assat, A. Iadecola, C. Delacourt, R. Dedryvère, J.-M. Tarascon, Decoupling Cationic-Anionic Redox Processes in a Model Li-Rich Cathode via Operando X-ray Absorption Spectroscopy. *Chemistry of Materials* **29**, 9714-9724 (2017).
- 777
- 778
- 779
78021. G. Assat, A. Iadecola, D. Foix, R. Dedryvère, J.-M. Tarascon, Direct Quantification of Anionic Redox over Long Cycling of Li-Rich NMC via Hard X-ray Photoemission Spectroscopy. *ACS Energy Letters* **3**, 2721-2728 (2018).
- 781
- 782
- 783
78422. K. Dai *et al.*, High Reversibility of Lattice Oxygen Redox Quantified by Direct Bulk Probes of Both Anionic and Cationic Redox Reactions. *Joule* **3**, doi: 10.1016/j.joule.2018.1011.1014 (2018).
- 785
- 786
78723. U. Maitra *et al.*, Oxygen redox chemistry without excess alkali-metal ions in Na_{2/3}[Mg_{0.28}Mn_{0.72}]O₂. *Nat Chem* **10**, 288-295 (2018).
- 788
78924. R. Qiao *et al.*, High-efficiency in situ resonant inelastic x-ray scattering (iRIXS) endstation at the Advanced Light Source. *Review of Scientific Instruments* **88**, 033106 (2017).
- 790
- 791
79225. F. Lin *et al.*, Synchrotron X-ray Analytical Techniques for Studying Materials Electrochemistry in Rechargeable Batteries. *Chemical Reviews*, (2017).
- 793
- 794
79526. Q. Li *et al.*, Quantitative probe of the transition metal redox in battery electrodes through soft x-ray absorption spectroscopy. *Journal of Physics D: Applied Physics* **49**, 413003 (2016).
- 796
- 797
79827. W. E. Gent *et al.*, Coupling between oxygen redox and cation migration explains unusual electrochemistry in lithium-rich layered oxides. *Nat Commun* **8**, 2091 (2017).
- 799
- 800
80128. J. Xu *et al.*, Elucidating anionic oxygen activity in lithium-rich layered oxides. *Nature Communications* **9**, 947 (2018).
- 802
80329. Z. Zhuo *et al.*, Spectroscopic Signature of Oxidized Oxygen States in Peroxides. *J Phys Chem Lett*, 6378-6384 (2018).
- 804
80530. S. M. Butorin, J. Guo, N. Wassdahl, E. J. Nordgren, Tunable-excitation soft X-ray fluorescence spectroscopy of high-T_c superconductors: an inequivalent-site seeing story. *Journal of Electron Spectroscopy and Related Phenomena* **110-111**, 235-273 (2000).
- 806
- 807
- 808
- 809
81031. Z. W. Lebens-Higgins *et al.*, Distinction between Intrinsic and X-ray-Induced Oxidized Oxygen States in Li-Rich 3d Layered Oxides and LiAlO₂. *The Journal of Physical Chemistry C* **123**, 13201-13207 (2019).
- 811
- 812

81332. X. Rong *et al.*, Structure-Induced Reversible Anionic Redox Activity in
814 Na Layered Oxide Cathode. *Joule* **2**, 125-140 (2018).
81533. K. Du *et al.*, Exploring reversible oxidation of oxygen in a manganese
816 oxide. *Energy & Environmental Science* **9**, 2575-2577 (2016).
81734. N. Yabuuchi *et al.*, New O2/P2-type Li-Excess Layered Manganese
818 Oxides as Promising Multi-Functional Electrode Materials for
819 Rechargeable Li/Na Batteries. *Advanced Energy Materials* **4**, 1301453
820 (2014).
82135. N. Yabuuchi *et al.*, A new electrode material for rechargeable sodium
822 batteries: P2-type Na_{2/3}[Mg_{0.28}Mn_{0.72}]O₂ with anomalously high
823 reversible capacity. *J. Mater. Chem. A* **2**, 16851-16855 (2014).
82436. N. Yabuuchi, Solid-state Redox Reaction of Oxide Ions for Rechargeable
825 Batteries. *Chemistry Letters* **46**, 412-422 (2016).
82637. R. Qiao *et al.*, Revealing and suppressing surface Mn(II) formation of
827 Na_{0.44}MnO₂ electrodes for Na-ion batteries. *Nano Energy* **16**, 186-195
828 (2015).
82938. W. Yang *et al.*, Key electronic states in lithium battery materials probed
830 by soft X-ray spectroscopy. *Journal of Electron Spectroscopy and
831 Related Phenomena Spectroscopy of Energy Materials* **190, Part A**, 64-
832 74 (2013).
83339. A. J. Achkar *et al.*, Bulk sensitive x-ray absorption spectroscopy free of
834 self-absorption effects. *Physical Review B* **83**, 081106 (2011).
83540. R. Qiao, T. Chin, S. J. Harris, S. Yan, W. Yang, Spectroscopic fingerprints
836 of valence and spin states in manganese oxides and fluorides. *Current
837 Applied Physics* **13**, 544-548 (2013).
83841. R. Qiao *et al.*, Direct evidence of gradient Mn(II) evolution at charged
839 states in LiNi_{0.5}Mn_{1.5}O₄ electrodes with capacity fading. *Journal of
840 Power Sources* **273**, 1120-1126 (2015).
84142. J. Xu *et al.*, Elucidating anionic oxygen activity in lithium-rich layered
842 oxides. *Nat Commun* **9**, 947 (2018).
84343. B. Song *et al.*, A novel P3-type Na_{2/3}Mg_{1/3}Mn_{2/3}O₂ as high capacity
844 sodium-ion cathode using reversible oxygen redox. *Journal of Materials
845 Chemistry A*, (2019).
84644. J. Wu *et al.*, Elemental-sensitive Detection of the Chemistry in Batteries
847 through Soft X-ray Absorption Spectroscopy and Resonant Inelastic X-
848 ray Scattering. *Journal of Visualized Experiments*, e57415 (2018).
84945. Y. D. Chuang *et al.*, Modular soft x-ray spectrometer for applications in
850 energy sciences and quantum materials. *Rev Sci Instrum* **88**, 013110
851 (2017).

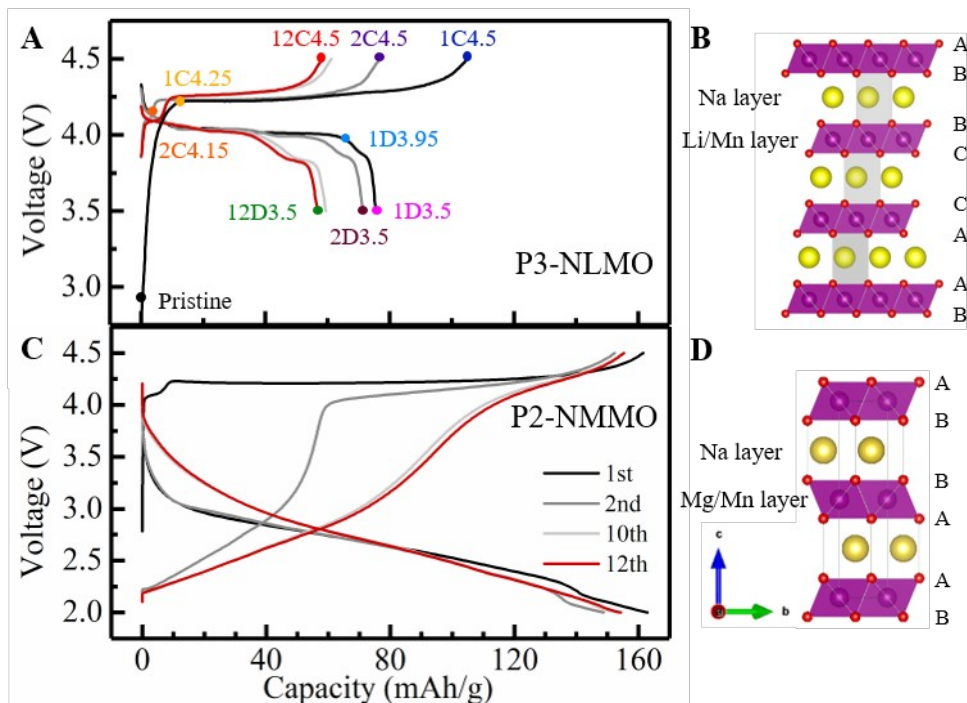
852 **Acknowledgments**

853 **Funding:** The Advanced Light Source is supported by the Director,
854 Office of Science, Office of Basic Energy Sciences, of the U.S.
855 Department of Energy under Contract No. DE-AC02-05CH11231. Works
856 at Stanford are supported by the Department of Energy, Office of
857 Science, Basic Energy Sciences, Materials Sciences and Engineering
858 Division, under Contract DE-AC02-76SF00515. Works at Berkeley are
859 partially supported by the Energy Biosciences Institute through the EBI-
860 Shell program. Works at Tsinghua are partially supported by China's
861 National Key R&D Programmes (2018YFB0905105). Some spectroscopic
862 analysis works are supported as part of the NorthEast Center for
863 Chemical Energy Storage (NECCES), an Energy Frontier Research
864 Center funded by Office of Science, Basic Energy Sciences, of the U.S.
865 Department of Energy under Award No. DE-SC0012583. J.W. would like
866 to thank the financial support of the ALS postdoctoral fellowship. The
867 authors thank Yongsheng Hu (IOP) and Xiqian Yu (IOP) for providing the
868 NLMO samples.
869

870 **Author contributions:** W.Y. and J.W. conceived the project and
871 coordinated collaborations with Z.S., R.Z., and Q.L. for contributions
872 from all authors. X.R. and Q.L. synthesized the NLMO materials and
873 conducted electrochemical tests. K.D. and G.L. synthesized NMMO
874 materials and conducted electrochemical tests. J.W., Z.Z., K.D., S.S. and
875 W.Y. performed spectroscopic measurements and analyzed the results.
876 J.W. and W.Y. wrote the manuscript with all authors reviewed and
877 contributed to the discussions.
878

879 **Competing Interests:** The authors declare that they have no
880 competing interests.
881

882 **Data and materials availability:** All data needed to evaluate the
883 conclusions in the paper are present in the paper and/or the
884 Supplementary Materials. Additional data related to this paper may be
885 requested from the authors.
886



888

889

890

891

892

893

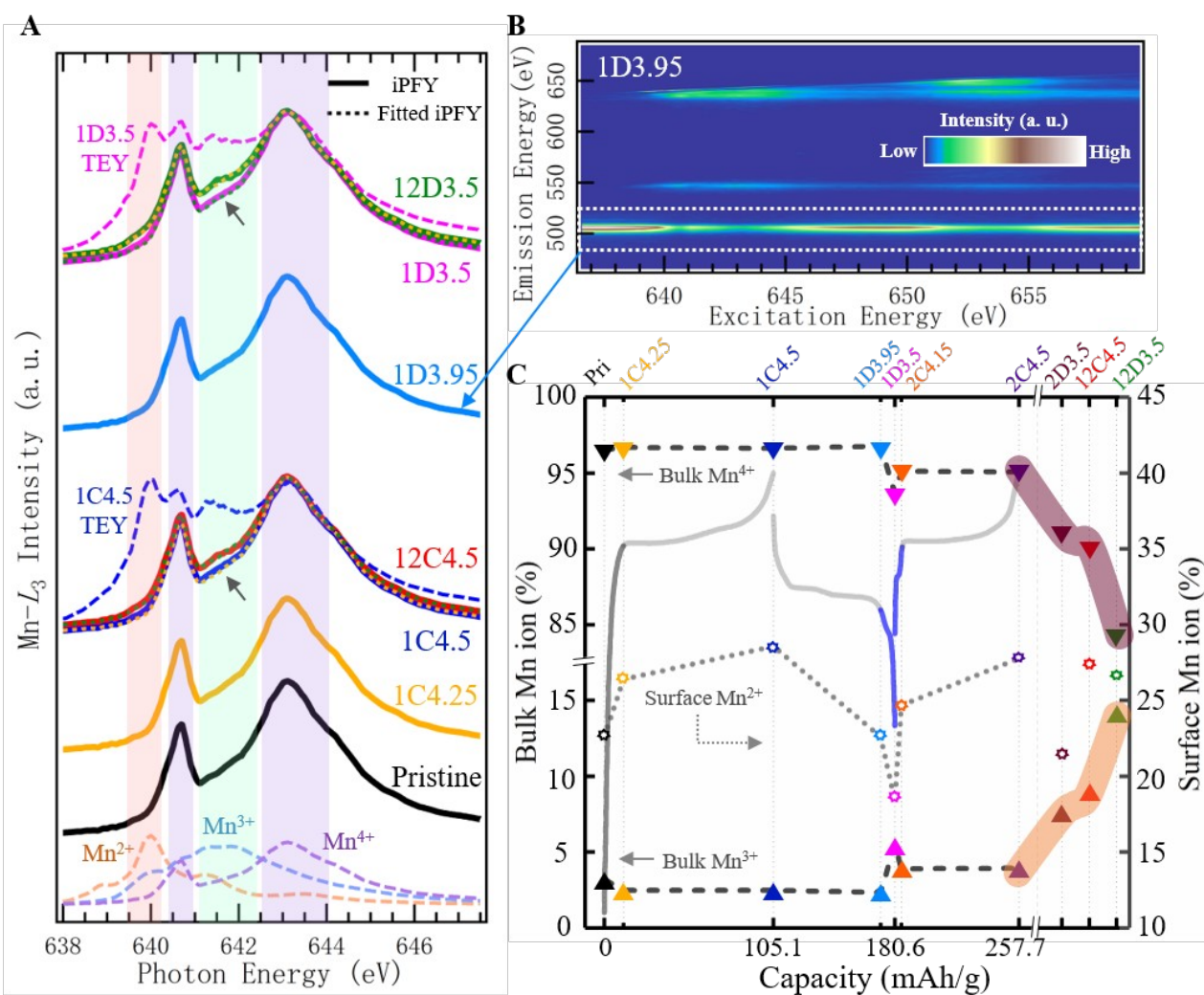
894

895

896

897

Fig. 1. Contrast between NLMO and NMMO system on capacity and voltage drops. (A) Electrochemical profile of NLMO/Na, 3.5 to 4.5V, 0.1C (10 mA g^{-1}). 10 presentative samples with different SOC's from multiple cycles were selected in this study. (B) P3-type layered structure of NLMO. (C) Electrochemical profile of NMMO/Na, 2.0 to 4.5V, 0.1C. (D) P2-type layered structure of NMMO with a different stacking.



898
 899
 900 **Fig. 2. Quantification of bulk and surface Mn oxidation states**
 901 **upon cycling.** (A) Mn- L_3 mRIXS-iPFY spectra as bulk probes (solid lines) and two typical TEY spectra of 1C4.5 and 1D3.5 as surface
 902 probes (dashed lines) of the Mn states. The mRIXS-iPFY are fitted precisely (dotted lines) via linear combination of the Mn^{2+/3+/4+}
 903 reference spectra (dashed lines at bottom), with the fitting results
 904 of all samples in Table 1. Data from the 12th cycle fully charged (12C4.5) and discharged (12D3.5) electrodes are plotted with the
 905 1st cycle data for direct comparison. Difference between the 1st
 906 and 12th cycle (grey arrows) indicates the accumulation of Mn³⁺
 907 upon cycling. (B) A typical Mn-L mRIXS collected from 1D3.95
 908 sample. The white frame indicates the area where iPFY is
 909 extracted by the inversed integration of the signals (see
 910 Methods). (C) The bulk Mn valence contents (left axis, triangles)
 911 and surface Mn²⁺ contents (right axis, circles) obtained through
 912 the quantitative fittings of the mRIXS-iPFY and sXAS-TEY spectra,
 913 respectively. Data are plotted upon cycling capacity with cycling
 914 profile over-plotted. Other than the representative results shown
 915 here, the sXAS, mRIXS, and mRIXS-iPFY (with fittings) of all
 916 samples are presented in Fig. S4, S5, and S6, respectively.
 917
 918
 919

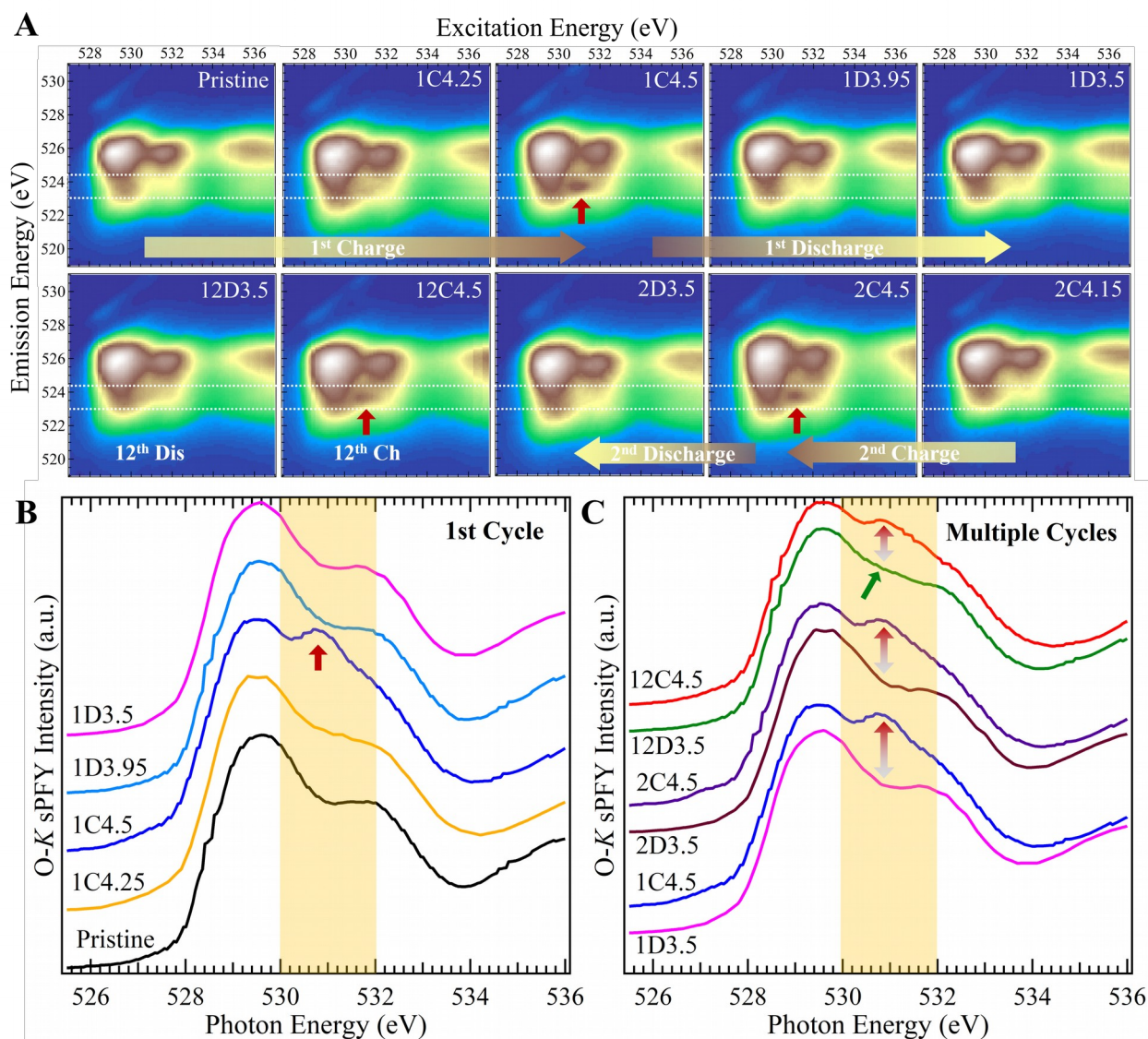


Fig. 3. O-K mRIXS and sPFY. (A) O-K mRIXS of NLMO electrodes at different electrochemical states. Red arrows indicate the oxidized oxygen feature at charged states, representing the lattice OR reactions (see text). Dotted lines on mRIXS images indicate the energy range for extracting sPFY spectra (see Methods). (B) O-K mRIXS-sPFY of 1st cycle, with area changes between 530-532 eV (shaded area) upon electrochemical cycling. (C) O-K mRIXS-sPFY of multiple cycles. The lattice OR contribution is reflected by the sPFY intensity difference within the shaded area between the charged and discharged electrodes, as indicated by double-arrows. Green arrow points to an obviously enhanced area at the 12th discharge, compared with the discharged states in the 1st and 2nd cycles.

921
922
923
924
925
926
927
928
929
930
931
932
933
934
935
936

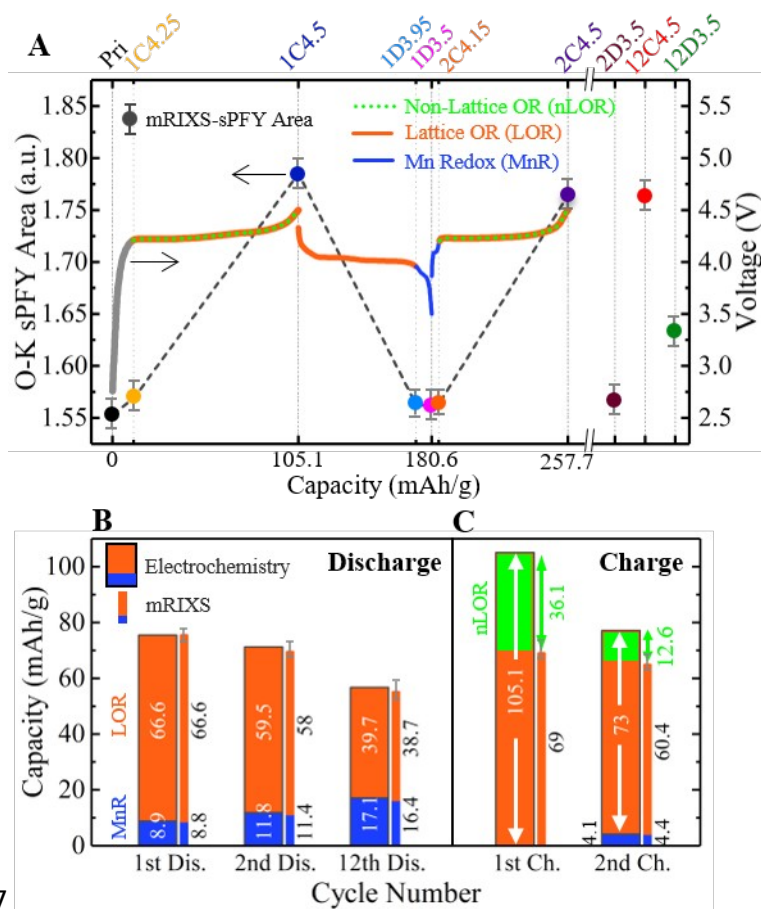


Fig. 4. Summary of quantification values of three different

redox reactions in NLMO. (A) The O-K mRIXS-sPFY peak area (dots and dashed lines, left axis) is plotted together with the cycling profile (right axis). Variations in sPFY peak area indicates the amount of lattice OR (LOR) reactions. Cycling profile is colored to show the three different kind of redox reactions at different voltage range, with red, blue and green (dotted) representing lattice OR, Mn, and non-lattice OR reactions, respectively. Note the range for Mn OR is also defined experimentally in Fig. 2C. (B) Two sets of capacity contributions of Mn redox (MnR, blue) and lattice O redox (LOR, red) during the 1st, 2nd and 12th discharge. Values of the framed wide columns are directly electrochemical capacities but with the lattice OR and Mn redox boundaries defined by mRIXS results (Fig. 2C, 4A). Capacity contribution values from “mRIXS” are calculated based on spectroscopic results themselves. Mn redox contribution is calculated based on the quantified Mn valence states (Table 1). Lattice OR contribution is quantified by the mRIXS-sPFY intensity change between charged and discharged states (Fig. 3C) with a conversion ratio (see text). The consistence between electrochemistry and mRIXS results validates that lattice OR dominates the discharging processes. (C) Two sets of capacity contributions of Mn redox (MnR, blue) and lattice O redox (LOR, red) during charging quantified through the same two methods

962 based on electrochemical capacity and mRIXS results. Unlike the
963 discharged states, the quantified LOR capacity from mRIXS is
964 dramatically smaller than the total OR capacity in
965 electrochemistry (white double arrows), indicating a large amount
966 of non-lattice oxygen redox (nLOR) during charge (green).
967

968 **Table 1. Contents of Mn valence states in bulk and on surface.**

969 Quantification values are based on fitting the Mn-L mRIXS-iPFY (for
 970 bulk) and sXAS-TEY (for surface) spectra. Capacity contribution of Mn
 971 redox (MnR) is then calculated directly based on the bulk Mn valence
 972 state changes. (Fitting results with standard deviations are in Table S1
 973 & S2.) Additionally, Mn capacity contribution from electrochemistry is
 974 obtained by extracting the capacity of the cycling profile in the range
 975 with Mn-L spectral changes (Fig. 2C).

	Surface Mn ²⁺ (%)	Bulk Mn ³⁺ (%)	Bulk Mn ⁴⁺ (%)		Mn charge transfer (mol)	Mn capacity contribution by mRIXS (mA·h/g)	Mn capacity contribution from electrochemistry (mA·h/g)
Pristine	22.58	3.21	96.53	1 st Charging	≈ 0.001	< 0.01	—
1C4.25	26.38	2.48	96.69				
1C4.5	28.57	2.48	96.64	1 st Discharging	0.030	8.8	8.9
1D3.95	22.58	2.34	96.77				
1D3.5	18.44	5.51	93.67	2 nd charging	0.015	4.4	4.1
2C4.15	24.68	3.89	95.11				
2C4.5	27.78	3.94	95.08	2 nd discharging	0.039	11.4	11.8
2D3.5	21.62	7.83	91.16				
12C4.5	27.47	9.03	90.28	12 th discharging	0.056	16.4	17.1
12D3.5	26.49	14.62	84.62				

976
977

978 **Table 2. Lattice and total OR capacities quantified through both**
 979 **electrochemical profile and mRIXS-sPFY area changes.** Changes
 980 of “O-K mRIXS-sPFY area” indicates the amount of lattice OR (Fig. 3C).
 981 Capacity contributions of lattice OR (LOR) is calculated based on sPFY
 982 area change with a conversion ratio of 303 mAh/g per area change (see
 983 text). The discharge process is dominated by LOR activities, however,
 984 LOR capacity during charge is much lower than the electrochemical
 985 capacities, indicating a significant amount of non-lattice oxygen redox
 986 (nLOR) during charge.

	O-K mRIXS-sPFY area (a.u.)	Std. Dev.		Area change (a.u.)	LOR capacity by mRIXS (mA·h/g)	Total OR capacity from electrochemistry (mA·h/g)	Ratio
Pristine	1.553	0.040					
1C4.25	1.599	0.065	1 st Charging	0.232	69.0	105.1	65.7%
1C4.5	1.785	0.052					
1D3.95	1.565	0.046	1 st Discharging	0.224	Benchmark: 66.6 (Capacity/Area = 66.6/0.224)	100%	
1D3.5	1.561	0.057					
2C4.15	1.571	0.055	2 nd charging	0.203	60.4	73.0	82.7%
2C4.5	1.764	0.052					
2D3.5	1.569	0.046	2 nd discharging	0.195	58.0	59.5	97.5%
12C4.5	1.763	0.052	12 th discharging	0.130	38.7	39.7	97.5%
12D3.5	1.633	0.064					

987
988